

Article

Structural Features of $Y_2O_2SO_4$ via DFT Calculations of Electronic and Vibrational Properties

Aleksandr S. Oreshonkov ^{1,2,*}  and Yuriy G. Denisenko ³ 

¹ Laboratory of Molecular Spectroscopy, Kirensky Institute of Physics, Federal Research Center KSC SB RAS, 660036 Krasnoyarsk, Russia

² School of Engineering and Construction, Siberian Federal University, 660041 Krasnoyarsk, Russia

³ Department of General and Special Chemistry, Industrial University of Tyumen, 625000 Tyumen, Russia; yu.g.denisenko@gmail.com

* Correspondence: oreshonkov@iph.krasn.ru

Abstract: The traditional way for determination of molecular groups structure in crystals is the X-Ray diffraction analysis and it is based on an estimation of the interatomic distances. Here, we report the analysis of structural units in $Y_2O_2SO_4$ using density functional theory calculations of electronic properties, lattice dynamics and experimental vibrational spectroscopy. The $Y_2O_2SO_4$ powder was successfully synthesized by decomposition of $Y_2(SO_4)_3$ at high temperature. According to the electronic band structure calculations, yttrium oxysulfate is a dielectric material. The difference between the oxygen–sulfur and oxygen–yttrium bond nature in $Y_2O_2SO_4$ was shown based on partial density of states calculations. Vibrational modes of sulfur ions and $[Y_2O_2^{2+}]$ chains were obtained theoretically and corresponding spectral lines observed in experimental Infrared and Raman spectra.

Keywords: yttrium oxysulfate; DFT; lattice dynamics; Infrared; Raman; vibrations; $Y_2O_2SO_4$



Citation: Oreshonkov, A.S.; Denisenko, Y.G. Structural Features of $Y_2O_2SO_4$ via DFT Calculations of Electronic and Vibrational Properties. *Materials* **2021**, *14*, 3246. <https://doi.org/10.3390/ma14123246>

Academic Editor: Jonathan Goss

Received: 17 May 2021
Accepted: 10 June 2021
Published: 11 June 2021

Publisher's Note: MDPI stays neutral with regard to jurisdictional claims in published maps and institutional affiliations.



Copyright: © 2021 by the authors. Licensee MDPI, Basel, Switzerland. This article is an open access article distributed under the terms and conditions of the Creative Commons Attribution (CC BY) license (<https://creativecommons.org/licenses/by/4.0/>).

1. Introduction

The rising in experimental and theoretical studies of rare-earth-activated phosphors over the past decades is primarily associated with their applications in lighting, electronic displays, temperature sensing, etc. [1]. A large variety of rare-earth doped inorganic compounds have been synthesized, such as molybdates [2–4], tungstates [5–7], phosphates [8–10], aluminates [11–13] and silicates [14–16].

Since the chemical formula contains trivalent rare-earth (Re^{3+}) ions, the common way for doping is a partial substitution of Re^{3+} with Ln^{3+} ($Ln^{3+} = Ce, Pr, Nd, Sm, Eu, Tb, Dy, Ho, Er, Tm, Yb, Lu$) ions. Recently, $Re_2O_2SO_4$ oxysulfate was studied as a host for optical materials and it has been shown that the luminescent efficiency of $Re_2O_2SO_4:Ln^{3+}$ phosphorous depends on the size and shape of particles [17], for example, the Eu^{3+} doped nanosized $Y_2O_2SO_4$ samples (18–89 nm, $C2/c$) show the quantum efficiencies ranging from $\eta = 44$ –70% [18]. The 2–3 μm in diameter $Y_2O_2SO_4:Eu^{3+}$ was synthesized using a urea-based homogeneous precipitation technique based on a urea-ammonium sulfate system [19]. The $Y_2O_2SO_4:Tb^{3+}$ microflakes were prepared via an electrospinning process followed by calcination treatment [20]. The biomolecule-assisted hydrothermal route followed by calcination was used for the production of yttrium oxysulfate hollow spheres doped with Yb^{3+} and Eu^{3+} or Er^{3+} [21].

Traditionally, the search of nonlinear optical (NLO) materials focused on borate systems [22], on the other hand, several NLO sulfate crystals were synthesized in recent years [23–27]. As to the $Re_2O_2SO_4$ oxysulfates, the crystal structure of $Nd_2O_2SO_4$ [28] was solved in the non-centrosymmetric ($I222$) space group and thus this class of compounds can be a candidate for NLO materials. On the other hand, the crystal structure of $Sm_2O_2SO_4$ [29] and $Eu_2O_2SO_4$ [30] was solved in the centrosymmetric ($C2/c$) space group.

Determination of non-centrosymmetric or centrosymmetric space groups in $Re_2O_2SO_4:Ln^{3+}$ can be easily done with Infrared spectroscopy as has been shown in work by Yu.G. Denisenko [30]. The focus of such study must be pointed to the presence of the peak related to the symmetric stretching vibration of SO_4 tetrahedra in case of the $C2/c$ space group. However, it should be noted that while the interpretation of the spectral peaks related to vibrations of sulfate groups is beyond doubt, vibrations of rare-earth ions were explained as just Y-O vibrations and detailed description of these vibrations is completely absent in the literature. The spectral bands at 1220, 1130, 1060, 1000, 880, 660 and 610 cm^{-1} were observed in Infrared spectra of $Y_2O_2SO_4:Eu^{3+}$ and attributed to vibrations of SO_4^{2-} ions, while the peak at 530 cm^{-1} was described as Y-O bond vibration [19]. In nanometer-sized $Y_2O_2SO_4:Eu^{3+}$, the Y-O bond peak was found at 560 cm^{-1} [31]. In Infrared spectra of $Y_2O_2SO_4$ doped with Tb^{3+} ions, characteristic spectral bands related to sulfate vibrations and the Y-O stretching (at 539 cm^{-1}) were observed [20]. Spectral peak related to the stretching vibrations of O-Y was found at 545 cm^{-1} in $Y_2O_2SO_4$ [32]. The spectral bands in $Y_2O_2SO_4$ nanoparticles at 1064, 1122, 133 and 664 have been attributed to SO_4^{2-} ions while bands at 621 and 534 to Y-O vibrations [33]. There is no information at all about Raman spectra.

In this paper, we report the synthesis of $Y_2O_2SO_4$, results of DFT (Density Functional Theory) calculations of electronic and vibrational properties and we demonstrated that spectral lines in Infrared and Raman spectra of $Y_2O_2SO_4$ were associated with $[SO_4]^{2-}$ and $[Y_2O_2]^{2+}$ structural units.

2. Materials and Methods

2.1. Synthesis and Experimental Details

Yttrium oxysulfate was obtained by decomposition of yttrium sulfate $Y_2(SO_4)_3$ (99.99%, Novosibirsk Rare Metals Plant, Novosibirsk, Russia) in an argon atmosphere at a temperature of 700 °C. A schematic of an installation for carrying out high temperature decomposition processes is shown in Figure 1. Argon of high purity 99.9999% was used to create an inert atmosphere. Temperature control and regulation was carried out using a microprocessor controller (“Thermokeramika”, Moscow, Russia). Temperature in the reaction zone was measured with a chromel-alumel thermocouple. A weighed portion of dry $Y_2(SO_4)_3$ was placed in a quartz reactor and purged with argon for 30 min at a rate of 6 L/h. After that, the reactor was placed in a heated vertical furnace and held for 10 h. After the completion of the reduction process, the reactor was removed from the furnace and cooled to room temperature. The decomposition recovery process is described by the equation:

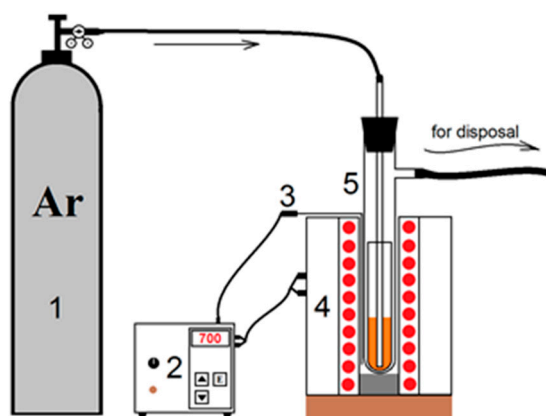
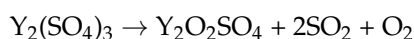


Figure 1. Installation for the synthesis of yttrium oxysulfate. 1—argon tank; 2—thermoregulator; 3—thermocouple; 4—vertical oven; 5—quartz reactor.

Fourier-transformed Infrared spectroscopy (IR) was carried out with the use of a Fourier Transform Infrared Spectrometer FSM 1201, (Infraspec Ltd., Borovliany, Minsk district, Belarus). The sample for the investigation was prepared in a tablet form with addition of annealed KBr. IR spectrum was recorded with spectral resolution 4 cm^{-1} . Raman spectrum was recorded using an i-Raman Plus spectrometer at a laser excitation wavelength of 785 nm and the spectral resolution was about 4 cm^{-1} . The Infrared as well as the Raman spectrum was obtained at room temperature.

2.2. Calculation Details

All the density functional theory calculations [34,35] were performed with the CASTEP code (version 19.1.1) [36]. The $4s^2 4p^6 4d^1 5s^2$, $3s^2 3p^4$ and $2s^2 2p^4$ valence electron configurations were used for Y, S and O, respectively. The local density approximation (LDA) based on the Perdew and Zunger parametrization [37] of the numerical results of Ceperley and Alder [38], and nonlocal exchange-correlation HSE06 functional [39] were used for calculation of electronic properties. The on-the-fly-generated norm-conserving pseudopotentials were used and the cutoff energy for the plane basis was chosen as 1150 eV . The convergence criteria for geometry optimization were set to $5.0 \times 10^{-4}\text{ eV}/\text{\AA}$ for maximal force and 0.01 GPa for maximal stress. The density functional perturbation theory (DFPT) (linear response method) [40] was used to perform the calculation of vibrational properties. Different k-point density [41] was checked for Monkhorst–Pack sampling [42] and it was found that the $6 \times 6 \times 3$ k-point set is enough.

3. Results and Discussion

Figure 2 presents the crystal structure of $\text{Y}_2\text{O}_2\text{SO}_4$. Investigated sulfate presents a monoclinic structure with the $C2/c$ space group (#15). As can be seen from Figure 2, the crystal structure consists of SO_4 layers and layers formed with Y and O ions. Calculated values of lattice parameters and atomic coordinates are presented in Table 1 and compared with experimental data from ICDD PDF 53-0168.

The Brillouin zone (BZ) of $\text{Y}_2\text{O}_2\text{SO}_4$ and electronic band structure obtained using the local density approximation are shown in Figure 3. The path along high symmetry points of BZ was selected as: $\Gamma\text{-C}|C_2\text{-Y}_2\text{-}\Gamma\text{-M}_2\text{-D}|D_2\text{-A-\Gamma}|L_2\text{-}\Gamma\text{-V}_2$. Coordinates of these points are: $\Gamma(0, 0, 0)$, $C(-0.276, 0.276, 0)$, $C_2(-0.724, -0.276, 0)$, $Y_2(-0.5, -0.5, 0)$, $M_2(-0.5, -0.5, 0.5)$, $D(-0.737, -0.263, 0.5)$, $D_2(-0.263, 0.263, 0)$, $A(0, 0, 0.5)$, $L_2(-0.5, 0, 0.5)$, $V_2(-0.5, 0, 0)$ (Figure 3a). The conduction band minimum (CBM) is located at the Γ point, while the valence band maximum (VBM) is located between M_2 and D k-point, thus making the $\text{Y}_2\text{O}_2\text{SO}_4$ an indirect band gap material, the $E_g^i = 5.32\text{ eV}$ (Figure 3b). However, the difference between indirect and direct electronic transition is small, the value of the calculated direct band gap is 5.37 eV . Taking into account that the experimental band gap value of $\text{Y}_2\text{O}_2\text{SO}_4$ has not yet been published and DFT calculations in LDA approximation generate a band structure which underestimates the gap [43], the electronic band structure was calculated using the HSE06 hybrid functional. The value of indirect and direct electronic transition obtained with HSE06 are 7.126 and 7.131 eV correspondingly. In the meantime, the electronic density of states (DOS) and partial DOS are shown in Figure 4. It is clearly seen from Figure 4 that the top of valence band is formed by p-electron of oxygen, while the bottom of the conduction band comprises Y's d-electrons. It is interesting to note that partial densities of states are different for oxygen ions in SO_4 tetrahedra and O1 ions located between Y layers (see Figure 2) and the VBM is formed with O1 atoms. Thus, the wide band gap dielectric behaviors ($E_g(\text{HSE06}) = 7.12\text{ eV}$) of $\text{Y}_2\text{O}_2\text{SO}_4$ are connected with the structural layer formed with Y and O1 atoms. The electronic density of states of O2 and O3 atoms (in SO_4 tetrahedra) from -8 to -6 eV has contribution from $2s$ and $2p$ orbitals while the same region is empty in DOS of O1. We suppose that, in this case, the DOS of O1 in the range of $-2.5\text{--}0\text{ eV}$ corresponds to the hybrid sp orbital, see Figure 4, and the OY_4 molecule can be distinguished as a separate structural unit, see Figure 5.

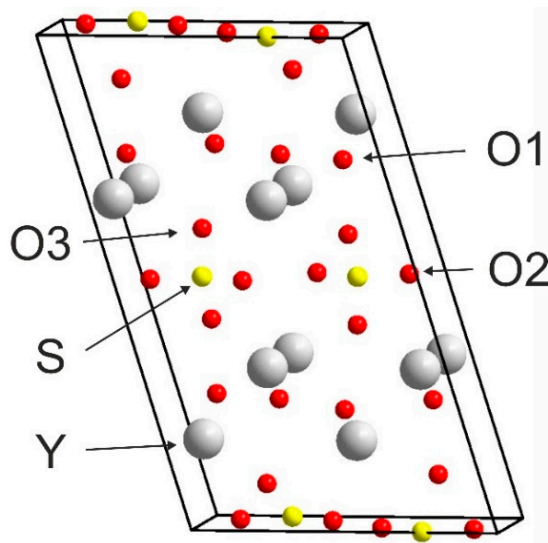


Figure 2. Conventional cell of $Y_2O_2SO_4$.

Table 1. DFT calculated structural parameters for $Y_2O_2SO_4$ in comparison to ICDD PDF 53-0168.

Lattice Dimensions, Å	a	b	c
Calc. (this work)	13.1242	4.0956	7.8734
ICDD PDF 53-0168	13.3076	4.1465	8.0204
Lattice Angles, Degrees	α, γ	β	
Calc. (this work)	90	107.292	
ICDD PDF 53-0168	90	107.64	
Fractional Coordinates	x	y	z
Y	0.17153	0.48979	0.08471
O1	0.24427	0.97988	0.12243
O2	0.9997	0.26714	0.09789
O3	0.09659	0.84802	0.29921
S	0	0.05146	0.25

The $Y_2O_2SO_4$ belongs to the monoclinic space group with the factor group symmetry C_{2h}^6 . Vibrational representation for the yttrium oxysulfate at the center of the Brillouin zone can be written as follow: $\Gamma_{\text{vibr}} = 13A_g + 13A_u + 14B_g + 14B_u$. The $A_u + 2B_u$ are acoustical translational modes while the remaining A_u and B_u modes are Infrared-active, the A_g and B_g are Raman-active vibrations. In the structure of $Y_2O_2SO_4$, the SO_4 tetrahedra occupy the positions with C_2 symmetry and relation between free $[SO_4]^{2-}$ ion with T_d symmetry, its site symmetry and the factor group symmetry of the monoclinic cell are presented in Table 2. According to Table 2, nine internal vibrations of SO_4 should be observed in Raman as in Infrared spectra. The Infrared and Raman spectra of $Y_2O_2SO_4$ are presented in Figure 6. The total set of observed spectral lines, DFT calculated wavenumbers and mode assignments are presented in Table 3.

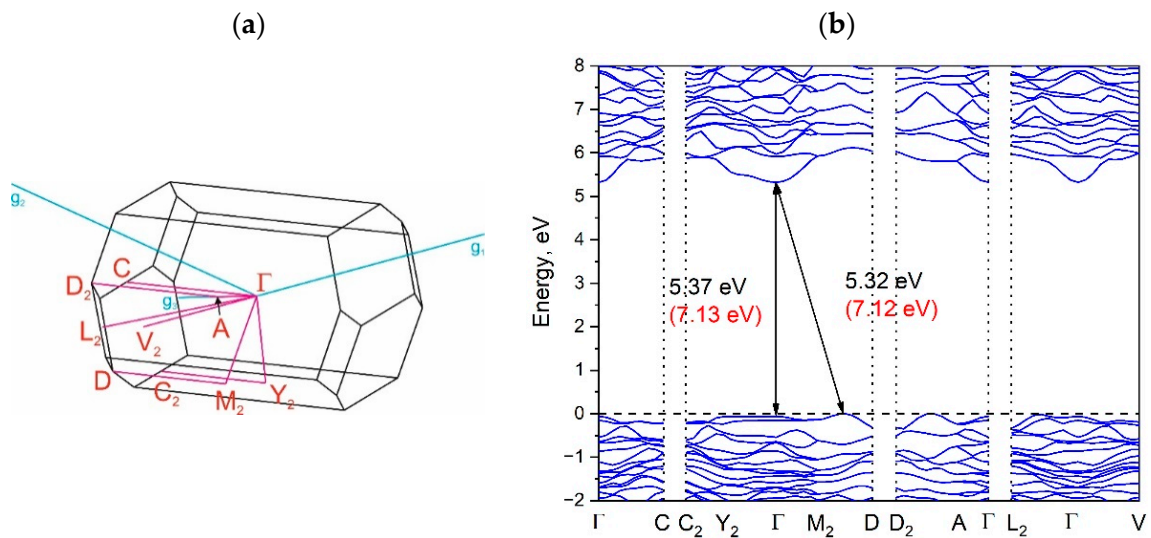


Figure 3. Brillouin zone (a) and electronic band structure (b) of $Y_2O_2SO_4$. Band gap values obtained with the hybrid functional are shown in parentheses in (b).

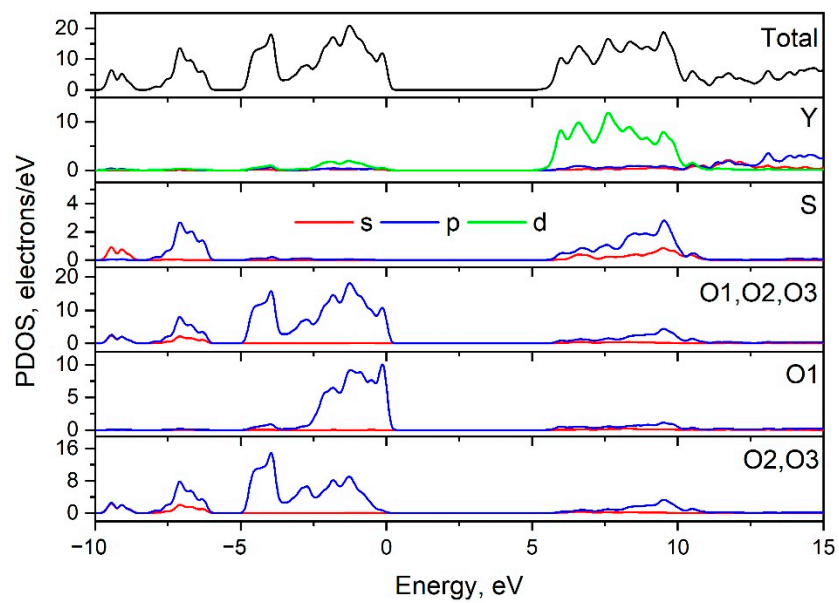


Figure 4. Total and partial density of electronic states of $Y_2O_2SO_4$.

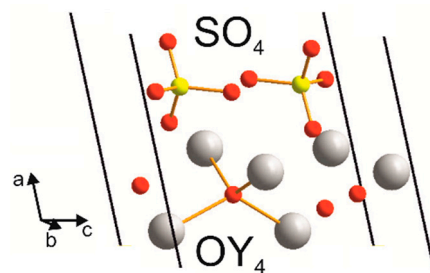
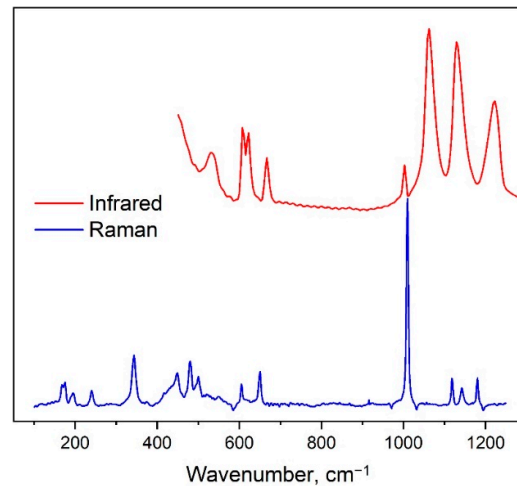


Figure 5. AB_4 ($A = S, O; B = O, Y$) structural units in $Y_2O_2SO_4$.

Table 2. Correlation between internal vibrations of SO₄ tetrahedra in Y₂O₂SO₄.

Wavenumber, cm ⁻¹ [44]	T _d	C ₂	C _{2h}
983	A ₁ (ν ₁)	A	A _g + A _u
450	E (ν ₂)	2A	2A _g + 2A _u
1105	F ₂ (ν ₃)	A+2B	A _g + A _u + 2B _g + 2B _u
611	F ₂ (ν ₄)	A+2B	A _g + A _u + 2B _g + 2B _u

**Figure 6.** Experimental Infrared and Raman spectra of Y₂O₂SO₄.**Table 3.** Calculated and experimental phonon wavenumbers (cm⁻¹) of Y₂O₂SO₄ with proposed assignments. Notations: Irreps.—irreducible representations, str.—stretching, tr.—translation, rot.—rotation, def.—deformation.

Infrared				Raman			
Irreps.	Calc	Exp	Assignment	Irreps.	Calc	Exp	Assignment
B _u	1155.6	1219		B _g	1154.3	1180	
A _u	1095.9	1133	ν ₃ SO ₄	B _g	1123.3	1142	ν ₃ SO ₄
B _u	1030.4	1063		A _g	1096.3	1118	
A _u	969.0	1002	ν ₁ SO ₄	A _g	980.0	1009	ν ₁ SO ₄
B _u	636.0	666		B _g	632.0	651	
B _u	592.1	621	ν ₄ SO ₄	B _g	629.3	648	ν ₄ SO ₄
A _u	581.9	608		A _g	584.3	604	
A _u	546.7		ν ₂ SO ₄ + O1-O1 str.	B _g	533.1	500	O1-O1 str.
B _u	499.1	532	O1 tr.	A _g	505.3	480	O1 tr.
A _u	481.7		ν ₂ SO ₄ + O1-O1 str.	B _g	492.9	448	O1-O1 str.
A _u	461.9		ν ₂ SO ₄	A _g	492.6	448	ν ₂ SO ₄
A _u	429.2		O1 tr.	A _g	476.2	432	ν ₂ SO ₄
B _u	416.3		O1 tr.	A _g	453.6	416	ν ₂ SO ₄ + O1-O1 str.
B _u	378.8		O1 tr.	B _g	383.2	374	O1-O1 tr.
A _u	334.3		O1 tr.	A _g	352.5	344	O1-O1 tr.
A _u	260.3		Y tr.	B _g	275.5		SO ₄ def.
B _u	231.2		SO ₄ rot.	A _g	248.3	240	Y tr.
B _u	216.2		SO ₄ rot.	B _g	240.2		Y tr.
A _u	191.3		SO ₄ rot.	B _g	207.7		SO ₄ tr.
B _u	187.4		SO ₄ tr.	B _g	203.1		SO ₄ tr.
B _u	157.7		SO ₄ tr.	A _g	202.1	195	SO ₄ rot.
A _u	151.6		SO ₄ def.	A _g	188.8		SO ₄ tr.
B _u	131.6		SO ₄ tr.	B _g	184.7		SO ₄ rot. + tr.
A _u	96.7		Y tr.	A _g	172.5	172	Y tr.
				B _g	161.2	168	SO ₄ tr.
				A _g	151.9		Y tr.
				B _g	120.0		SO ₄ tr. + [Y ₂ O ₂ ²⁺] tr.

The weak spectral band at 969 cm⁻¹ in the Infrared spectrum and strongest band at 1009 cm⁻¹ in the Raman spectrum are associated with ν₁ symmetric stretching vibrations

of SO_4 groups. Spectral bands above 1000 cm^{-1} are antisymmetric stretching vibrations (ν_3). Bands at 650 and 604 cm^{-1} in Raman spectrum are ν_4 antisymmetric bending of SO_4 tetrahedra. The ν_4 modes appeared in the Infrared spectrum at 666 , 621 and 608 cm^{-1} . Spectral lines in Raman spectrum at 448 and 432 cm^{-1} are defined as ν_2 symmetric bending of sulfur ions. The rotational vibration of SO_4 appeared in Raman spectrum as the peak at 195 cm^{-1} . The Raman peak at 168 cm^{-1} is explained as translations of SO_4 in the SO_4 structural layer.

Connection of the OY_4 tetrahedra (Figure 5) into the chains creates the $[\text{Y}_2\text{O}_2^{2+}]$ layers as shown in Figure 7 and vibrations of these layers have been found in Raman spectra. Spectral band at 500 cm^{-1} is related to O-O stretching, as shown in Figure 8a. The line at 480 cm^{-1} is an antiphase translation of O atoms along the layer, Figure 8b. The spectral line at 374 cm^{-1} is an antiphase vibration of O in $[\text{Y}_2\text{O}_2^{2+}]$ structural units as shown in Figure 8c. The strong band at 344 cm^{-1} is an antiphase vibration of O atoms, Figure 8d. The A_u mode (Infrared active) with a calculated wavenumber value equal to 546.7 cm^{-1} is a combination of ν_2 vibrations of SO_4 and O-O stretching, as shown in Figure 8e. The B_u mode at 499.1 cm^{-1} is a translation of O, as shown in Figure 8f. Thus, we can conclude that the wide spectral band at 532 cm^{-1} in Infrared spectra is devoted to oxygen vibration in $[\text{Y}_2\text{O}_2^{2+}]$ chains, but not to Y-O vibrations as was stated earlier [19,20,31–33]. The assignment of remain vibrational modes is presented in Table 3.

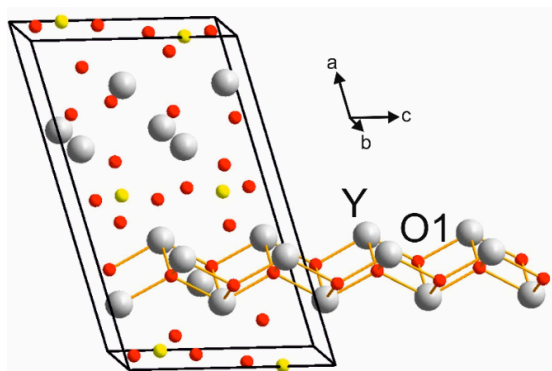


Figure 7. Representation of $[\text{Y}_2\text{O}_2^{2+}]$ layers in crystal structure of $\text{Y}_2\text{O}_2\text{SO}_4$.

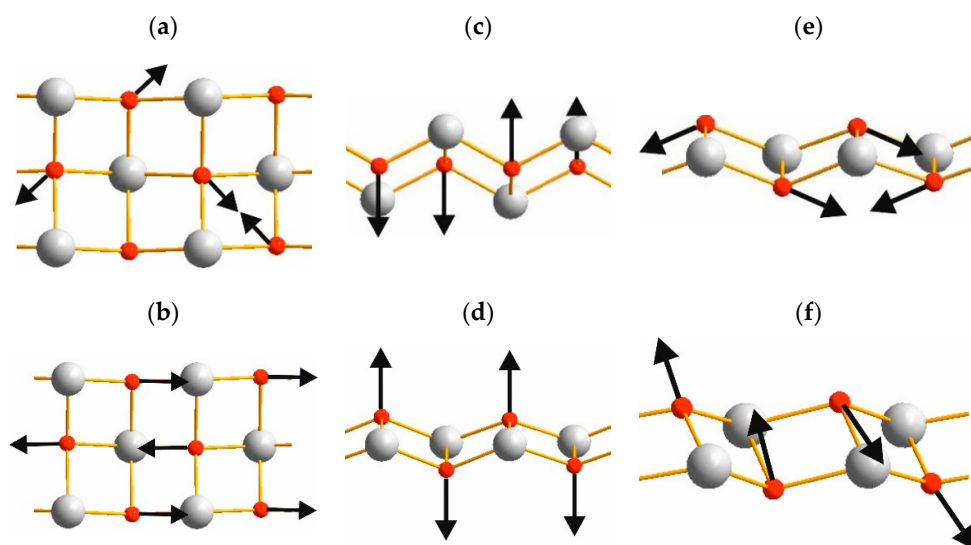


Figure 8. Representative atomic vibrations of $[\text{Y}_2\text{O}_2^{2+}]$ chains in $\text{Y}_2\text{O}_2\text{SO}_4$: (a) B_g 533.1 cm^{-1} , (b) A_g 505.3 cm^{-1} , (c) B_g 383.2 cm^{-1} , (d) A_g 352.5 cm^{-1} , (e) A_u 546.7 cm^{-1} , (f) B_u 499.1 cm^{-1} .

4. Conclusions

In summary, we have demonstrated that the lines in vibrational spectra of $\text{Y}_2\text{O}_2\text{SO}_4$ should be interpreted in terms of vibrations of SO_4 tetrahedra and layers composed of $[\text{Y}_2\text{O}_2^{2+}]$ structural units. Calculated partial density of states shows different electron distribution for s and p orbitals in case of oxygen atoms in $[\text{SO}_4]^{2-}$ and in case of $[\text{Y}_2\text{O}_2^{2+}]$. The formation of hybrid sp orbital in yttrium–oxygen chains is supposed. The electronic structure and band gap value of yttrium oxysulfate was presented for the first time.

Author Contributions: Conceptualization, A.S.O.; formal analysis, A.S.O. and Y.G.D.; investigation, A.S.O. and Y.G.D.; resources, Y.G.D.; writing—original draft preparation, A.S.O.; project administration, A.S.O. All authors have read and agreed to the published version of the manuscript.

Funding: This research received no external funding.

Institutional Review Board Statement: Not applicable.

Informed Consent Statement: Not applicable.

Data Availability Statement: The data presented in this study are available on request from the corresponding author.

Conflicts of Interest: The authors declare no conflict of interest.

References

1. Qin, X.; Liu, X.; Huang, W.; Bettinelli, M.; Liu, X. Lanthanide-activated phosphors based on 4f-5d optical transitions: Theoretical and experimental aspects. *Chem. Rev.* **2017**, *117*, 4488–4527. [[CrossRef](#)]
2. Lim, C.S.; Aleksandrovsky, A.; Atuchin, V.; Molokeev, M.; Oreshonkov, A. Microwave-employed sol–gel synthesis of scheelite-type microcrystalline $\text{AgGd}(\text{MoO}_4)_2:\text{Yb}^{3+}/\text{Ho}^{3+}$ upconversion yellow phosphors and their spectroscopic properties. *Crystals* **2020**, *10*, 1000.
3. Lim, C.S.; Aleksandrovsky, A.S.; Atuchin, V.V.; Molokeev, M.S.; Oreshonkov, A.S. Microwave sol-gel synthesis, microstructural and spectroscopic properties of scheelite-type ternary molybdate upconversion phosphor $\text{NaPbLa}(\text{MoO}_4)_3:\text{Er}^{3+}/\text{Yb}^{3+}$. *J. Alloys Compd.* **2020**, *826*, 152095. [[CrossRef](#)]
4. Lim, C.S.; Aleksandrovsky, A.S.; Molokeev, M.S.; Oreshonkov, A.S.; Atuchin, V.V. Microwave synthesis and spectroscopic properties of ternary scheelite-type molybdate phosphors $\text{NaSrLa}(\text{MoO}_4)_3:\text{Er}^{3+}, \text{Yb}^{3+}$. *J. Alloys Compd.* **2017**, *713*, 156–163. [[CrossRef](#)]
5. Lim, C.S.; Atuchin, V.V.; Aleksandrovsky, A.S.; Denisenko, Y.G.; Molokeev, M.S.; Oreshonkov, A.S. Fabrication of microcrystalline $\text{NaPbLa}(\text{WO}_4)_3:\text{Yb}^{3+}/\text{Ho}^{3+}$ phosphors and their upconversion photoluminescent characteristics. *Korean J. Mater. Res.* **2019**, *29*, 741–746. [[CrossRef](#)]
6. Lim, C.S.; Aleksandrovsky, A.; Molokeev, M.; Oreshonkov, A.; Atuchin, V. Microwave sol–gel synthesis and upconversion photoluminescence properties of $\text{CaGd}_2(\text{WO}_4)_4:\text{Er}^{3+}/\text{Yb}^{3+}$ phosphors with incommensurately modulated structure. *J. Solid State Chem.* **2015**, *228*, 160–166. [[CrossRef](#)]
7. Otsuka, T.; Brehl, M.; Cicconi, M.R.; de Ligny, D.; Hayakawa, T. Thermal evolutions to glass-ceramics bearing calcium tungstate crystals in borate glasses doped with photoluminescent Eu^{3+} ions. *Materials* **2021**, *14*, 952. [[CrossRef](#)] [[PubMed](#)]
8. Zhao, F.; Song, Z.; Liu, Q. Color-tunable persistent luminescence of $\text{Ca}^{10}\text{M}(\text{PO}_4)_7:\text{Eu}^{2+}$ (M = Li, Na, and K) with a $\beta\text{-Ca}_3(\text{PO}_4)_2$ -Type Structure. *Inorg. Chem.* **2021**, *60*, 3952–3960. [[CrossRef](#)]
9. Wu, H.; Li, H.; Jiang, L.; Pang, R.; Zhang, S.; Li, D.; Liu, G.; Li, C.; Feng, J.; Zhang, H. Synthesis, structure and optical properties of novel thermally robust Dy^{3+} -doped $\text{Ca}_9\text{Sc}(\text{PO}_4)_7$ phosphors for NUV-excited white LEDs. *J. Rare Earth.* **2021**, *39*, 277–283. [[CrossRef](#)]
10. Dahiya, M.; Siwach, A.; Dalai, M.; Kumar, D. Study of structural and luminescent characteristics of novel color tunable blue-green Tb^{3+} -doped $\text{Na}_3\text{Y}(\text{PO}_4)_2$ nanoparticles for NUV-based WLEDs. *J. Mater. Sci. Mater. Electron.* **2021**, *32*, 4166–4176.
11. Zhai, B.; Xu, H.; Huang, Y.M. Annealing temperature dependent afterglow of Tb^{3+} doped CaAl_2O_4 . *Opt. Mater.* **2021**, *112*, 110739. [[CrossRef](#)]
12. Singh, M.N.; Barua, A.G.; Gartia, R.K. Thermoluminescence studies of Tm doped nanocrystalline Calcium Aluminate ($\text{CaAl}_2\text{O}_4:\text{Tm}^{3+}$). *Optik* **2021**, *228*, 166151. [[CrossRef](#)]
13. Shivaramu, N.J.; Coetsee, E.; Roos, W.D.; Nagabhushana, K.R.; Swart, H.C. Charge carrier trapping processes in un-doped and $\text{BaAl}_2\text{O}_4:\text{Eu}^{3+}$ nanophosphor for thermoluminescent dosimeter applications. *J. Phys. D Appl. Phys.* **2020**, *53*, 475305. [[CrossRef](#)]
14. Yin, Z.; Yuan, P.; Zhu, Z.; Li, T.; Yang, Y. Pr^{3+} doped $\text{Li}_2\text{SrSiO}_4$: An efficient visible-ultraviolet C up-conversion phosphor. *Ceram. Int.* **2021**, *47*, 4858–4863. [[CrossRef](#)]
15. Shinde, V.V.; Tiwari, A.; Dhoble, S.J. Synthesis of RE^{3+} ($\text{RE}^{3+} = \text{Ce}^{3+}, \text{Dy}^{3+}, \text{Eu}^{3+}$ and Tb^{3+}) activated Gd_2SiO_5 optoelectronics materials for lighting. *J. Mol. Struct.* **2020**, *1217*, 128397. [[CrossRef](#)]

16. Xie, L.; Luo, D.; Zhu, Y.; Xu, C.; Chen, G.-X.; Xu, R.-J.; Zhou, X.-Q.; Li, Y. Monitoring of hydroxyapatite conversion by luminescence intensity and color during mineralization of Sm^{3+} -doped β -dicalcium silicate. *J. Lumin.* **2020**, *226*, 117468. [[CrossRef](#)]
17. Xu, G.X.; Lian, J.B.; Wu, N.C.; Zhang, X.; He, J. Co-precipitation synthesis of $\text{La}_2\text{O}_2\text{SO}_4:\text{Tb}^{3+}$ phosphor and its conversion to $\text{La}_2\text{O}_2\text{S}:\text{Tb}^{3+}$ ceramic scintillator via pressureless sintering in hydrogen. *J. Ceram. Sci. Technol.* **2018**, *9*, 345–352.
18. Silva, I.G.N.; Morais, A.F.; Brito, H.F.; Mustafa, D. $\text{Y}_2\text{O}_2\text{SO}_4:\text{Eu}^{3+}$ nano-luminophore obtained by low temperature thermolysis of trivalent rare earth 5-sulfoisophthalate precursors. *Ceram. Int.* **2018**, *44*, 15700–15705. [[CrossRef](#)]
19. Li, X.; Lian, J. Synthesis and characterizations of pompon-like $\text{Y}_2\text{O}_2\text{SO}_4:\text{Eu}^{3+}$ phosphors using a UBHP technique based on UAS system. *Optik* **2016**, *127*, 401–406. [[CrossRef](#)]
20. Xing, T.H.; Song, L.X.; Xiong, J.; Cao, H.B.; Du, P.F. Preparation and luminescent properties of Tb^{3+} doped $\text{Y}_2\text{O}_2\text{SO}_4$ microflakes. *Adv. Appl. Ceram.* **2013**, *112*, 455–459. [[CrossRef](#)]
21. Chen, G.; Chen, F.; Liu, X.; Ma, W.; Luo, H.; Li, J.; Ma, R.; Qiu, G. Hollow spherical rare-earth-doped yttrium oxysulfate: A novel structure for upconversion. *Nano Res.* **2014**, *7*, 1093–1102. [[CrossRef](#)]
22. Oreshonkov, A.S.; Roginskii, E.M.; Shestakov, N.P.; Gudim, I.A.; Temerov, V.L.; Nemtsev, I.V.; Molokeev, M.S.; Adichtchev, S.V.; Pugachev, A.M.; Denisenko, Y.G. Structural, electronic and vibrational properties of $\text{YAl}_3(\text{BO}_3)_4$. *Materials* **2020**, *13*, 545. [[CrossRef](#)] [[PubMed](#)]
23. Wu, C.; Lin, L.; Wu, T.; Huang, Z.; Zhang, C. Deep-ultraviolet transparent alkali metal–rare earth metal sulfate $\text{NaY}(\text{SO}_4)_2 \cdot \text{H}_2\text{O}$ as a nonlinear optical crystal: Synthesis and characterization. *CrystEngComm* **2021**, *23*, 2945. [[CrossRef](#)]
24. Liu, H.; Wu, Q.; Liu, L.; Lin, Z.; Halasyamani, P.S.; Chen, X.; Qin, J. $\text{AgBi}(\text{SO}_4)(\text{IO}_3)_2$: Aliovalent substitution induces structure dimensional upgrade and second harmonic generation enhancement. *Chem. Commun.* **2021**, *57*, 3712. [[CrossRef](#)]
25. Li, Y.; Liang, F.; Zhao, S.; Li, L.; Wu, Z.; Ding, Q.; Liu, S.; Lin, Z.; Hong, M.; Luo, J. Two non- π -conjugated deep-UV nonlinear optical sulfates. *J. Am. Chem. Soc.* **2019**, *141*, 3833–3837. [[CrossRef](#)]
26. Chen, K.; Yang, Y.; Peng, G.; Yang, S.; Yan, T.; Fan, H.; Lin, Z.; Ye, N. $\text{A}_2\text{Bi}_2(\text{SO}_4)_2\text{Cl}_4$ ($\text{A} = \text{NH}_4, \text{K}, \text{Rb}$): Achieving a subtle balance of the large second harmonic generation effect and sufficient birefringence in sulfate nonlinear optical materials. *J. Mater. Chem. C* **2019**, *7*, 9900. [[CrossRef](#)]
27. Netzsch, P.; Bariss, H.; Bayarjargal, L.; Höpfe, H.A. $\text{Tb}(\text{HSO}_4)(\text{SO}_4)$ —A green emitting hydrogensulfate sulfate with second harmonic generation response. *Dalton Trans.* **2019**, *48*, 16377. [[CrossRef](#)]
28. Golovnev, N.N.; Molokeev, M.S.; Vereshchagin, S.N.; Atuchin, V.V. Synthesis and thermal transformation of a neodymium(III) complex $[\text{Nd}(\text{HTBA})_2(\text{C}_2\text{H}_3\text{O}_2)(\text{H}_2\text{O})_2] \cdot 2\text{H}_2\text{O}$ to non-centrosymmetric oxosulfate $\text{Nd}_2\text{O}_2\text{SO}_4$. *J. Coord. Chem.* **2015**, *68*, 1865–1877. [[CrossRef](#)]
29. Denisenko, Y.G.; Sal'nikova, E.I.; Basova, S.A.; Molokeev, M.S.; Krylov, A.S.; Aleksandrovsky, A.S.; Oreshonkov, A.S.; Atuchin, V.V.; Volkova, S.S.; Khritokhin, N.A.; et al. Synthesis of samarium oxysulfate $\text{Sm}_2\text{O}_2\text{SO}_4$ in the high-temperature oxidation reaction and its structural, thermal and luminescent properties. *Molecules* **2020**, *25*, 1330. [[CrossRef](#)] [[PubMed](#)]
30. Denisenko, Y.G.; Molokeev, M.S.; Krylov, A.S.; Aleksandrovsky, A.S.; Oreshonkov, A.S.; Azarapin, N.O.; Plyusnin, P.E.; Sal'nikova, E.I.; Andreev, O.V. High-temperature oxidation of europium (II) sulfide. *J. Ind. Eng. Chem.* **2019**, *79*, 62–70. [[CrossRef](#)]
31. Lian, J.; Qin, H.; Liang, P.; Liu, F. Co-precipitation synthesis of $\text{Y}_2\text{O}_2\text{SO}_4:\text{Eu}^{3+}$ nanophosphor and comparison of photoluminescence properties with $\text{Y}_2\text{O}_3:\text{Eu}^{3+}$ and $\text{Y}_2\text{O}_2\text{S}:\text{Eu}^{3+}$ nanophosphors. *Solid State Sci.* **2015**, *48*, 147–154. [[CrossRef](#)]
32. Song, L.; Shao, X.; Du, P.; Cao, H.; Hui, Q.; Xing, T.; Xiong, J. A facile preparation and the luminescent properties of Eu^{3+} -doped $\text{Y}_2\text{O}_2\text{SO}_4$ nanopieces. *Mater. Res. Bull.* **2013**, *48*, 4896–4900. [[CrossRef](#)]
33. Shafaie, F.; Hadadzadeh, H.; Behnamfar, M.T.; Rudbari, H.A. Electrocatalytic activity of a mononuclear yttrium(III)-methyl orange complex and $\text{Y}_2\text{O}_2\text{SO}_4$ nanoparticles for adsorption/desorption of hydrogen. *Mater. Chem. Phys.* **2016**, *184*, 222–232. [[CrossRef](#)]
34. Hohenberg, P.; Kohn, W. Inhomogeneous electron gas. *Phys. Rev.* **1964**, *136*, B864–B871. [[CrossRef](#)]
35. Kohn, W.; Sham, L.J. Self-consistent equations including exchange and correlation effects. *Phys. Rev.* **1965**, *140*, A1133–A1138. [[CrossRef](#)]
36. Clark, S.J.; Segall, M.D.; Pickard, C.J.; Hasnip, P.J.; Probert, M.I.J.; Refson, K.; Payne, M.C. First principles methods using CASTEP. *Z. Kristallogr.* **2005**, *220*, 567–570. [[CrossRef](#)]
37. Perdew, J.P.; Zunger, A. Self-interaction correction to density-functional approximations for many-electron systems. *Phys. Rev. B.* **1981**, *23*, 5048. [[CrossRef](#)]
38. Ceperley, D.M.; Alder, B.J. Ground state of the electron gas by a stochastic method. *Phys. Rev. Lett.* **1980**, *45*, 566. [[CrossRef](#)]
39. Krukau, A.V.; Vydrov, O.A.; Izmaylov, A.F.; Scuseria, G.E. Influence of the exchange screening parameter on the performance of screened hybrid functionals. *J. Chem. Phys.* **2006**, *125*, 224106. [[CrossRef](#)]
40. Baroni, S.; de Gironcoli, S.; Corso, A.D.; Giannozzi, P. Phonons and related crystal properties from density-functional perturbation theory. *Rev. Mod. Phys.* **2001**, *73*, 515–562. [[CrossRef](#)]
41. Deng, Z.; Li, Z.; Wang, W.; She, J. Vibrational properties and Raman spectra of pristine and fluorinated blue phosphorene. *Phys. Chem. Chem. Phys.* **2019**, *21*, 1059–1066. [[CrossRef](#)] [[PubMed](#)]
42. Monkhorst, H.J.; Pack, J.D. Special points for Brillouin-zone integrations. *Phys. Rev. B.* **1976**, *13*, 5188–5192. [[CrossRef](#)]
43. Perdew, J.P. Density functional theory and the band gap problem. *Int. J. Quantum Chem.* **1986**, *19*, 497–523. [[CrossRef](#)]
44. Nakamoto, K. *Infrared and Raman Spectra of Inorganic and Coordination Compounds*, 6th ed.; Wiley: New York, NY, USA, 2009.